High-Fidelity Numerical Study of In-Line Excitation Force Estimation for Wave Energy Converters

Shangyan Zou, Ossama Abdelkhalik, Mohamed A. Shabara
Department of Aerospace Engineering
Iowa State University, Ames, IA, 50011 USA

***Abstract*—The wave excitation force is required in some control algorithms of wave energy converters. Excitation force is not, however, directly measurable. Therefore, to obtain excitation force information for control implementation, a number of excitation force estimators have been developed. The estimation performance is usually validated by low-fidelity simulations. This paper assesses the performance of a wave estimator in a Computational Fluid Dynamics (CFD) based Numerical Wave Tank (CNWT), where the estimator collects necessary measurements inline with the high-fidelity simulation. The proposed simulation framework can be directly applied for a controlled wave energy converter. Numerical simulations are conducted on the implemented estimator, and the estimated excitation force is compared with a benchmark force that is extracted from a diffraction test.**

***Index Terms*—Excitation Force Estimation; Nonlinear Kalman Filter; Numerical Wave Tank; Wave Energy Conversion; Computational Fluid Dynamics**

I. Introduction

Renewable energy is a clean, efficient, and inexhaustive alternative to conventional fossil energy. Ocean wave energy has attracted increasing research attention recently due to its high power density, and reliability [1]. However, it is relatively under-developed compared to other renewable energy sources (particularly wind and solar, which are already commercialized). In the last few decades, significant research progress has been made on developing the dynamics and control of wave energy converters. In most studies, it was shown that a control designed in an optimal sense would require the knowledge of the excitation force [2]–[4]. To that end, a number of excitation force estimators have been developed in the literature [5]–[8]. Multiple reviews about the state-of-the-art excitation force estimation techniques are presented in [8]–[11]. These developed estimators (thoroughly reviewed and compared in [8]) can be classified according to the applied Wave Energy Converter (WEC) dynamics (e.g., estimators use linear WEC model [9], [10], [12] and use nonlinear WEC model [6], [9]). Typically, integrated with a estimator is a model for the excitation force, which is usually based on potential flow theory. These estimators are usually tested in a low-fidelity simulator, which, in turn, also uses numerical models that are based on potential flow theory (linear/weakly nonlinear). In practice, the WEC dynamics are expected to significantly differ from the model (linear/weakly nonlinear) applied in the estimators, especially when the motion of the device is significantly excited by the control, the shape of device is highly nonlinear, the motion in different degrees of freedom are heavily coupled, and/or the incoming wave is large. Therefore, it is necessary and of high interest to the community to study the performance of the developed estimators in high-fidelity simulations (fully nonlinear) (which is a common practice for analyzing excitation force estimation). Giving that the implemented WEC model is fully nonlinear, it is thus of interest to apply and assess the performance of a nonlinear excitation force estimator (the nonlinear estimator that is developed in-house by the authors [6] will be applied in this paper). A relative moderate wave condition and a 'geometrically-linear' [13] WEC (cylindrical) are applied in the simulations such that the potential flow theory is still applicable to evaluate the pressure distribution on the wetted surface. Moreover, the control is not introduced in this stage (free-motion [14]) to concentrate on analyzing the performance of the estimator.

CFD-based Numerical Wave Tanks [15]–[17] has been used in the literature for high-fidelity simulations. High-fidelity simulations are widely served as the platform for varied applications including mooring line analysis [18], control analysis [19], and excitation force estimator analysis [8] which is the focus of this paper. ANSYS® and OpenFOAM are both widely applied in developing numerical wave tanks [20]. The ANSYS Fluent [21] is adopted in this paper to perform the high-fidelity simulations. A series of user-defined functions (UDFs are written in C) are developed for the implemented estimator, which are coupled with the Fluent simulations. Unlike most of the developed estimators (assume excitation force is the superposition of sinusoidal components [22]), the implemented nonlinear estimator (developed in [6]) applies a weakly nonlinear model. In which the excitation force is computed by integrating hydrodynamic pressures in the wet surface. As far as the measurements are concerned, extra pressure sensor measurements are collected to improve the accuracy of the estimation in addition to typical position and velocity measurements.

The paper ID is 2054, and it is submitted to the conference track: Grid integration, PTO & control.

Shangyan Zou is a Postdoctoral Researcher, shangyan@iastate.edu
Ossama Abdelkhalik is Associate Professor, ossama@iastate.edu
Mohamed A. Shabara is a Graduate Research Assistant, mshabara@iastate.edu

This paper presents the performance of excitation force estimation of a nonlinear estimator in a high-fidelity simulator. A Computational Fluid Dynamics based Numerical Wave Tank (CNWT) is developed for the high-fidelity simulation with the estimator collecting the measurements in-line from the free motion response (unlike reference [8] which collect measurements from diffraction test). The proposed simulation framework gives a convincing assessment of the performance of estimators and can be later used for optimal control implementation. Additionally, the performance of the estimator is numerically analyzed, compared, and thoroughly discussed with the presented simulation results. The paper is organized as follows: the numerical methodology is introduced in Section. II, and the simulation results are presented in Section. III. The conclusion is drawn in Section. IV.

II. Numerical Modelling

A. Dynamic Modelling

The dynamic behavior of the cylindrical WEC is simulated in a CNWT simulator. As shown in Fig. 1, the proposed computational domain has the length of 80m (x-direction), the width of 60m (y-direction), and the height of 60m (z-direction). The WEC has a height of 4m, a radius of 1.5m, and a mass of 14137.17kg. Initially, the center of gravity ($(40,\ 30,\ 40)$m) of the device is located at the equilibrium, which is also the Free Surface Level (FSL). The test incoming wave has a Bretchneider wave spectrum with a peak period of 6s and a significant wave height of 0.4m. Additionally, since this paper focuses on assessing the performance of the excitation force estimator (only free/uncontrolled motion will be simulated), the Power Take-Off (PTO) system will not be modelled in this paper. In the simulation, there is no constraint on the degree of motion. Since the flow current velocity is assumed to be zero, it is expected the heave motion will be the dominant motion of the cylindrical WEC.

1) Governing Equations: To model ocean conditions, two phases (including air and water) are applied in the simulator. Assuming the fluids are incompressible, the mass and momentum conservation are used as governing equations:

$$\begin{aligned}&\frac{\partial \rho}{\partial t} + \Delta \cdot (\rho \vec{v}) = 0\\ &\frac{\partial}{\partial t}(\rho \vec{v}) + \Delta \cdot (\rho \vec{v}\vec{v}) = -\Delta p + \Delta \cdot (\bar{\bar{\tau}}) + \rho \vec{g} + \vec{F}\end{aligned} \tag{1}$$

In this equation, ρ and $\vec{v}$ are the fluid density and velocity, respectively. Additionally, p is the static pressure and $\bar{\bar{\tau}}$ is the stress tensor, and $\rho\vec{g}$ is the gravitational body force. $\vec{F}$ represents the additional source introduced by the Numerical Beach Treatment (NBT) in the momentum conservation. The governing equations are discretized over the fluid domain by using the finite volume method, and the Reynolds Averaged Navier Stokes (RANS) method is applied as the transient solver.

The k-epsilon model [23] is applied as the turbulence model, and the transport equations for turbulent kinetic energy (k) and dissipation rate (ϵ) will be solved.

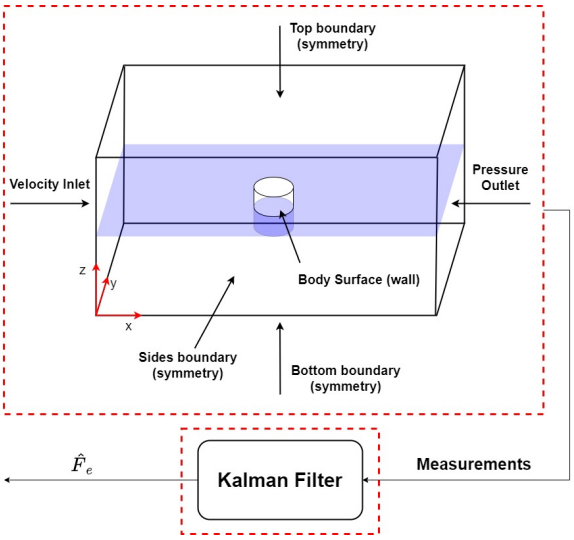

Fig. 1: The boundary conditions applied in this numerical wave tank. In the proposed simulation framework, the estimators collect the measurements in-line from the CFD simulation.

Further, The multi-phase flow is simulated by using the Volume of Fluid (VOF) model, in which air and water are defined as primary phase and secondary phase, respectively. The interface between these two phases is tracked by the volume fraction equation:

$$\frac{\partial(\alpha_q)\rho_q}{\partial t} + \Delta \cdot (\alpha_q \rho_q \vec{v}_q) = 0 \tag{2}$$

where ρ_q and $\vec{v}_q$ is the density and velocity of the qth fluid, respectively. α_q is the volume fraction of qth fluid (obeys $\sum_{q=1}^{N} \alpha_q = 1$) which only varies between 0 (cell is empty of phase q) and 1 (cell is full of phase q). Furthermore, a negative diffusion source term is added in the volume fraction equation to further sharpen the interface between air and water.

A diffusion-based dynamic mesh smoothing method [23] is applied to account for the large mesh motion. In addition, the Coupled algorithm is used as the pressure-velocity coupling scheme to achieve aggressive convergence in this unsteady simulation. The second-order upwind scheme is selected for the spatial discretization algorithm of momentum and turbulence, and the second-order implicit is the applied transient formulation.

2) Domain and Boundary Conditions: The boundary conditions applied in the simulation are introduced in Fig. 1. The ocean waves are generated from the velocity inlet, which has the downstream at the pressure outlet. Symmetry boundary conditions are applied for top, bottom, and sides of the control volume, which represents an open sea condition (deep water and infinite air). Additionally, the non-slip wall is used as the boundary condition of the body surface. As far as the ocean wave is concerned, the irregular wave is generated based on the superposition of linear waves:

$$\zeta(x,t) = \sum_{n=1}^{N} a_n \cos(k_n x - \omega_n t + \phi_n) \tag{3}$$

where a_n and ϕ_n are the wave elevation and random phase shift of nth wave, respectively. The wavenumber

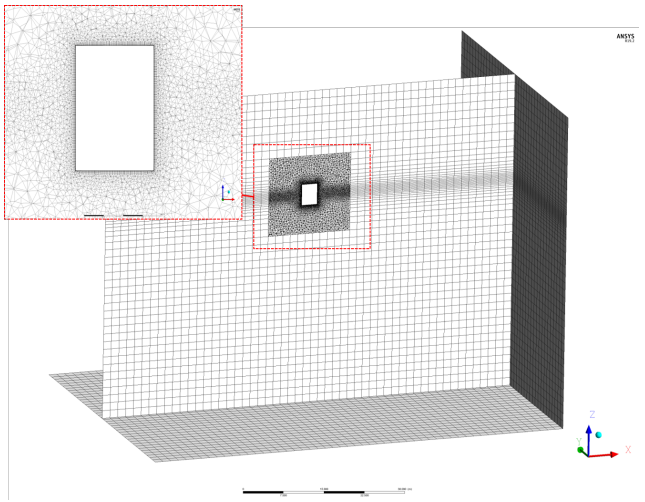

Fig. 2: The mesh generation of the overall control volume.

k_n can be computed by applying dispersion relation for deep water waves (assumed 60m water depth): $k_n = \omega_n^2/g$. The wave direction is assumed to be 0^o in this simulation. Therefore the spatial distribution of the wave is only influenced by the x coordinate. Further, the flow current velocity is assumed to be 0m/s; the wave frequency ω_n is thus directly applied in the above equation as the effective wave frequency. In this paper, the ω_n of the irregular wave (20 frequencies in total) is evenly distributed from 0.5rad/s to 2rad/s.

To suppress the wave reflection from the downstream and the sides of the CNWT, a multi-direction NBT is enabled by adding a damping sink term ($\vec{F}$) in the momentum equation. The NBT is located at the pressure outlet and sides boundaries and has a length of 20m, 10m, and 10m, respectively. The associated linear damping resistance is 55.92s^{-1} and quadratic damping resistance is 3334.48m^{-1}.

B. Mesh Generation

A hybrid meshing strategy is applied in this paper, which applies unstructured mesh to track the geometry of the device and structured mesh in the background to save computational cost. As shown in Fig. 2, the mesh is refined in the fluid domain that is closer to the device (which has a box shape) with an element size of 0.5m, and the mesh in the background has an element size of 1.5m. It is also clearly visible that the mesh is refined on the expected free surface with an element size of 0.2m. Considering extra accuracy is required in the boundary layer region to capture the rapid velocity change, the mesh is refined on the surface of the device with an element size of 0.08m, and inflation layers are also placed in this region (more clearly seen in the zoom-in scope). The minimum volume and the minimum face area of the generated mesh are $3.7 \times 10^{-6}\text{m}^3$ and $1.5 \times 10^{-4}\text{m}^2$. In addition, the total mesh element count is 1214344, with approximately 90% mesh elements distributed in the refined fluid domain (box shape) and the rest distributed in the background.

C. Nonlinear Kalman Filter

The implemented nonlinear Kalman Filter is first introduced and validated in [6] (with low-fidelity models). This paper further assesses the performance of the developed Continuous-Discrete Extended Kalman Filter (CDEKF) with high-fidelity simulations. A weakly nonlinear model is implemented in the CDEKF:

$$\begin{aligned}
\dot{\hat{x}}_1 &= \hat{x}_2 \\
\dot{\hat{x}}_2 &= \frac{1}{M}(\hat{F}_e + \hat{F}_B + \hat{F}_r - B_v\hat{x}_2 - m_r g) \\
\dot{\hat{\vec{x}}}_r &= \mathbf{A}_r\hat{\vec{x}}_r + \mathbf{B}_r\hat{x}_2 \\
\dot{\hat{a}}_n = 0, &\quad \dot{\hat{\omega}}_n = 0, \quad \dot{\hat{\phi}}_n = 0, \quad n = 1, 2, 3...N_w
\end{aligned} \tag{4}$$

where in this equation $\hat{x}_1$ and $\hat{x}_2$ represent the estimations of the displacement and velocity. $M = m_r + A_\infty$ is the total mass including the rigid body mass and the frequency independent added mass. The expected total force acting on the device includes the excitation force ($\hat{F}_e$), the buoyancy force ($\hat{F}_B$), the radiation force ($\hat{F}_r$), the viscous damping force ($-B_v\hat{x}_2$), and gravity force. It is noted that the excitation force neglects the effect of diffraction force since the dynamic Froude Krylov force is the dominant component [2]. As shown in above equation, the radiation force can be approximated by a state space model and the resulting force thus is: $\hat{F}_r = -C_r\hat{\vec{x}}_r$. In this equation, $\hat{\vec{x}}_r$ represents the estimation of radiation states. The radiation matrices ($\mathbf{A}_r$, $\mathbf{B}_r$, and $\mathbf{C}_r$) can be identified from the radiation damping and added mass calculated from Nemoh. Furthermore, the buoyancy force can expressed as the surface integration of the hydrostatic pressure: $\hat{F}_B = \sum_{j=1}^{N_f} A_j(-\rho g(\hat{x}_1 + z_j))$ and the excitation force can also be written as the surface integration of the hydrodynamic pressure:

$$\begin{aligned}
\hat{F}_e = &\sum_{j=1}^{N_f} A_j \sum_{n=1}^{N_w} (\rho g \hat{a}_n e^{k_n(\hat{x}_1 + z_j)} \\
&\cos(k_n x_j - \hat{\omega}_n t + \hat{\phi}_n))
\end{aligned} \tag{5}$$

Since the device used in this paper has a cylindrical shape, the pressures are only integrated on the bottom of the device (only heave motion is considered). The hydrostatic and hydrodynamic pressures are evaluated on each face cell of the bottom face and jth face cell has a centroid location of (x_j, y_j, z_j) and a face area of A_j. In addition, $\hat{a}_n$, $\hat{\omega}_n$, and $\hat{\phi}_n$ are the estimations of the wave elevation, wave frequency, and random phase shift, and k_n is calculated based on dispersion relation for deep water. Defining the estimated state vector as: $\hat{\vec{x}} = [\hat{x}_1, \hat{x}_2, \hat{\vec{x}}_r, \hat{\vec{a}}, \hat{\vec{\omega}}, \hat{\vec{\phi}}]^T$. The Jacobian matrix for the nonlinear dynamics can be therefore computed in Eq. 6; where

$$\begin{aligned}
\left.\frac{\partial f_2}{\partial x_1}\right|_{\hat{\vec{x}}} = &\frac{1}{M}(\sum_{j=1}^{N_f} A_j \sum_{n=1}^{N_w} (\rho g a_n k_n e^{k_n(\hat{x}_1 + z_j)} \\
&\cos(k_n x_j - \hat{\omega}_n t + \hat{\phi}_n)) + \sum_{j=1}^{N_f} A_j \rho g)
\end{aligned} \tag{8}$$

$$\left.\frac{\partial f_2}{\partial x_2}\right|_{\hat{\vec{x}}} = -\frac{B_v}{M} \tag{9}$$

$$\mathbf{F} = \begin{bmatrix} 0 & 1 & \mathbf{0}^{1\times N_r} & \mathbf{0}^{1\times N_w} & \mathbf{0}^{1\times N_w} & \mathbf{0}^{1\times N_w} \\ \frac{\partial f_2}{\partial x_1} & \frac{\partial f_2}{\partial x_2} & \frac{\partial f_2}{\partial \vec{x}_r} & \frac{\partial f_2}{\partial a_1}\cdots\frac{\partial f_2}{\partial a_{N_w}} & \frac{\partial f_2}{\partial \omega_1}\cdots\frac{\partial f_2}{\partial \omega_{N_w}} & \frac{\partial f_2}{\partial \phi_1}\cdots\frac{\partial f_2}{\partial \phi_{N_w}} \\ \mathbf{0}^{N_r\times 1} & \frac{\partial \mathbf{f}_r}{\partial x_2} & \frac{\partial \mathbf{f}_r}{\partial \vec{x}_r} & \mathbf{0}^{N_r\times N_w} & \mathbf{0}^{N_r\times N_w} & \mathbf{0}^{N_r\times N_w} \\ \mathbf{0}^{3N_w\times 1} & \mathbf{0}^{3N_w\times 1} & \mathbf{0}^{3N_w\times N_r} & \mathbf{0}^{3N_w\times N_w} & \mathbf{0}^{3N_w\times N_w} & \mathbf{0}^{3N_w\times N_w} \end{bmatrix}\Bigg|_{\hat{\vec{x}}} \tag{6}$$

$$\mathbf{H} = \begin{bmatrix} 1 & 0 & \mathbf{0}^{1\times N_r} & \mathbf{0}^{1\times N_w} & \mathbf{0}^{1\times N_w} & \mathbf{0}^{1\times N_w} \\ 0 & 1 & \mathbf{0}^{1\times N_r} & \mathbf{0}^{1\times N_w} & \mathbf{0}^{1\times N_w} & \mathbf{0}^{1\times N_w} \\ \frac{\partial \vec{p}}{\partial x_1} & \frac{\partial \vec{p}}{\partial x_2} & \frac{\partial \vec{p}}{\partial \vec{x}_r} & \frac{\partial \vec{p}}{\partial a_1}\cdots\frac{\partial \vec{p}}{\partial a_{N_w}} & \frac{\partial \vec{p}}{\partial \omega_1}\cdots\frac{\partial \vec{p}}{\partial \omega_{N_w}} & \frac{\partial \vec{p}}{\partial \phi_1}\cdots\frac{\partial \vec{p}}{\partial \phi_{N_w}} \end{bmatrix}\Bigg|_{\hat{\vec{x}}_k^-} \tag{7}$$

$$\left.\frac{\partial f_2}{\partial \vec{x}_r}\right|_{\hat{\vec{x}}} = -\frac{\mathbf{C}_r}{M} \tag{10}$$

$$\left.\frac{\partial f_2}{\partial a_n}\right|_{\hat{\vec{x}}} = \frac{1}{M}\sum_{j=1}^{N_f} A_j(\rho g e^{k_n(\hat{x}_1+z_j)} \cos(k_n x_j - \hat{\omega}_n t + \hat{\phi}_n)) \quad n = 1,2,3...N_w \tag{11}$$

$$\left.\frac{\partial f_2}{\partial \omega_n}\right|_{\hat{\vec{x}}} = \frac{1}{M}\sum_{j=1}^{N_f} A_j(\rho g \hat{a}_n e^{k_n(\hat{x}_1+z_j)} t\sin(k_n x_j - \hat{\omega}_n t + \hat{\phi}_n)) \quad n = 1,2,3...N_w \tag{12}$$

$$\left.\frac{\partial f_2}{\partial \phi_n}\right|_{\hat{\vec{x}}} = -\frac{1}{M}\sum_{j=1}^{N_f} A_j(\rho g \hat{a}_n e^{k_n(\hat{x}_1+z_j)} \sin(k_n x_j - \hat{\omega}_n t + \hat{\phi}_n)) \quad n = 1,2,3...N_w \tag{13}$$

$$\left.\frac{\partial \mathbf{f}_r}{\partial x_2}\right|_{\hat{\vec{x}}} = \mathbf{B}_r \tag{14}$$

$$\left.\frac{\partial \mathbf{f}_r}{\partial \vec{x}_r}\right|_{\hat{\vec{x}}} = \mathbf{A}_r \tag{15}$$

In addition to the measurements of displacement and velocity, wave pressure measurements are also collected by multiple pressure sensors installed on the hull of the device. The details of the experimental installation of these sensors can be found in [6]. In this paper, 4 pressure sensors are applied and located at [38.5, 30, 38.5]m, [38.5, 30, 39]m, [38.5, 30, 39.5]m, and [38.5, 30, 40]m (measured from global coordinate system as shown in Fig. 1). Therefore, the measurement vector can be defined as:

$$y_m = [x_1,\, x_2,\, p_1,\, p_2,\, p_3,\, p_4]^T + \vec{v} \tag{16}$$

where the wave pressure p_j at certain location (e.g., pressure sensor locations) is formulated as:

$$p_j = \sum_{n=1}^{N_w} \rho g a_n e^{k_n(x_1+z_j)} \cos(k_n x_j - \omega_n t + \phi_n) - \rho g(x_1 + z_j) - \frac{B_v x_2}{A} - \frac{\mathbf{C}_r \vec{x}_r}{A} \tag{17}$$

It is noted that the radiation pressure and viscous damping pressure are assumed to be evenly distributed on the wet surface. Accordingly, their average pressures (force divided by the cross-sectional area of the cylinder as shown in Eq. (17)) are applied as the components of total wave pressure at the location of pressure sensors. The Jacobian matrix for the output model is then computed by Eq. (7). In this equation, the partial derivatives are expressed as:

$$\left.\frac{\partial p_j}{\partial x_1}\right|_{\hat{\vec{x}}_k^-} = \sum_{n=1}^{N_w} \rho g \hat{a}_{n,k}^- k_n e^{k_n(\hat{x}_{1,k}^- + z_j)} \cos(k_n x_j - \hat{\omega}_{n,k}^- t + \hat{\phi}_{n,k}^-) - \rho g \tag{18}$$

$$\left.\frac{\partial p_j}{\partial x_2}\right|_{\hat{\vec{x}}_k^-} = -\frac{B_v}{A} \tag{19}$$

$$\left.\frac{\partial p_j}{\partial \vec{x}_r}\right|_{\hat{\vec{x}}_k^-} = -\frac{\mathbf{C}_r}{A} \tag{20}$$

$$\left.\frac{\partial p_j}{\partial a_n}\right|_{\hat{\vec{x}}_k^-} = \rho g e^{k_n(\hat{x}_{1,k}^- + z_j)} \cos(k_n x_j - \hat{\omega}_{n,k}^- t + \hat{\phi}_{n,k}^-) \tag{21}$$

$$\left.\frac{\partial p_j}{\partial \omega_n}\right|_{\hat{\vec{x}}_k^-} = \rho g \hat{a}_{n,k}^- e^{k_n(\hat{x}_{1,k}^- + z_j)} t \sin(k_n x_j - \hat{\omega}_{n,k}^- t + \hat{\phi}_{n,k}^-) \tag{22}$$

$$\left.\frac{\partial p_j}{\partial \phi_n}\right|_{\hat{\vec{x}}_k^-} = -\rho g \hat{a}_{n,k}^- e^{k_n(\hat{x}_{1,k}^- + z_j)} \sin(k_n x_j - \hat{\omega}_{n,k}^- t + \hat{\phi}_{n,k}^-) \tag{23}$$

The initial guess of the proposed CDEKF can be evaluated by applying available wave information. In addition to initialize the estimation of the displacement ($\hat{x}_{10}$), velocity ($\hat{x}_{20}$), and radiation states ($\vec{\hat{x}}_{r0}$) as 0.1, the estimation of the wave elevation ($\vec{\hat{a}}_0$) and phase shift ($\vec{\hat{\phi}}_0$) can be initialized by interpolating the true wave information with less number of frequencies ($\vec{\hat{\omega}}_0$ evenly distributed in the same range of the true wave frequencies). The implementation of CDEKF is well-documented in [24], which will not be addressed in this paper. It is noted that a significant model mismatch is expected between the weakly nonlinear hydrodynamics used in the estimation and the CNWT simulation. Therefore, it is necessary to assume a large process noise covariance noise ($\mathbf{Q}$).

III. Simulation Results and Discussion

Numerical simulations are conducted to validate the performance of the proposed estimator, and the estimated excitation force will be presented and compared with a diffraction test. Considering the high computational cost of CNWT simulation, the High-Performance Computer (HPC) at Iowa State University is applied to carry out the simulations. The time step is selected as 0.005s to keep the flow courant number close to 1.

A validation of the developed simulator is first conducted (with a unit height and 6s period regular wave)

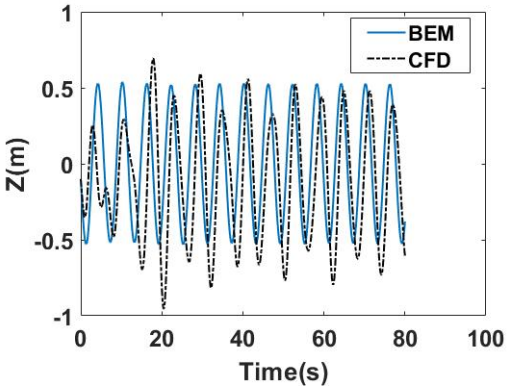

Fig. 3: Comparison between the displacement predicted by the CFD and the linear model (denoted as BEM).

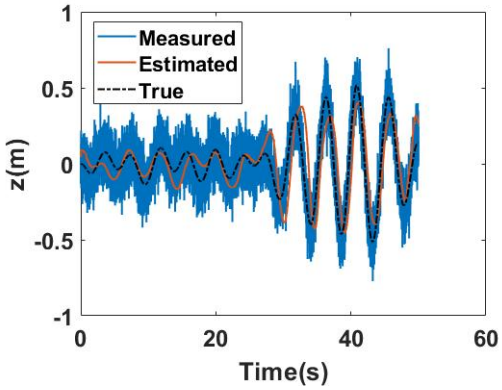

Fig. 4: The comparison between estimated, measured, and true displacement by using the nonlinear estimator.

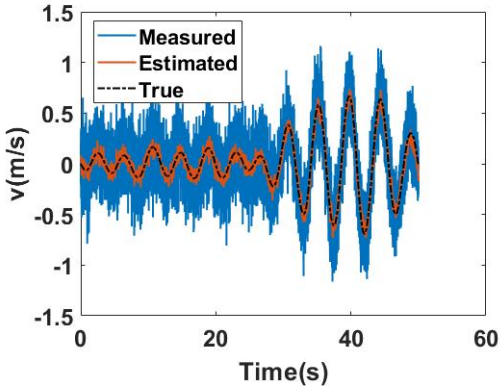

Fig. 5: The comparison between estimated, measured, and true velocity by using the nonlinear estimator.

by comparing the system response that is predicted by a low-fidelity linear model (denoted as Boundary Element Method (BEM) in Fig. 3) with a high-fidelity model (denoted as CFD in Fig. 3). The simulation result is consistent with the literature [25], [26].

The estimation of the displacement and velocity are shown in Fig. 4 and 5. In the figures, the true signal denotes the actual displacement and velocity, the measured signal denotes the measurements collected from the environment (true signal with measurement noise), and the estimated signal represents the estimation of the true signal. The estimation has a good tracking of the true signal subject to large measurement noise. The details of the estimations of the wave components (one element of $\hat{\vec{a}}$, $\hat{\vec{\omega}}$, and $\hat{\vec{\phi}}$) are shown in Fig. 6. The

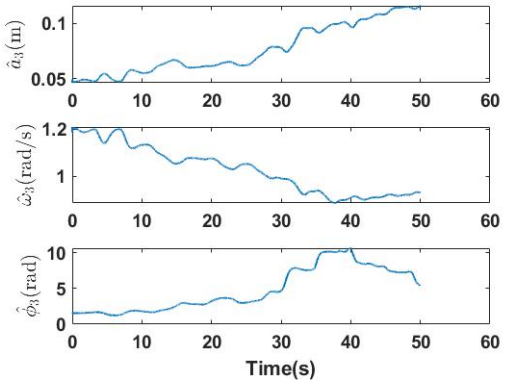

Fig. 6: The estimation of the wave components (a, ω, and ϕ) of the excitation force by using the nonlinear estimator.

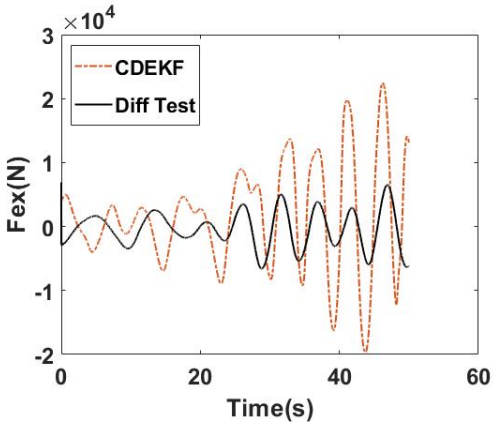

Fig. 7: The comparison between the excitation force estimated by the nonlinear estimator and the benchmark diffraction test (denoted as Diff Test).

performance of excitation force estimation is shown in Fig. 7. Considering there is no true excitation force that can be measured in practice (neither the CNWT simulation), a diffraction test [8] is conducted by holding the buoy, and the measured wave force (after removing the hydrostatic component) can be used as the benchmark. It is clearly visible that the excitation force estimated by the nonlinear estimator is significantly larger than the force extracted from the diffraction test. It is worth noting that the force extracted from the diffraction test neglects the influence of the motion (in order to eliminate other motion-dependent forces, e.g., radiation force). While the true excitation force is actually motion dependent (as shown in the exponential term in Eq. (5) when using potential flow theory). This dependency is more significant when the motion is relatively large. Considering that the system responses in the presented numerical experiments are relatively small, the motion independent force extracted from the diffraction test is reasonably close to the true excitation force. Therefore it is possible to conclude the presented nonlinear Kalman Filter overestimates the excitation force. This was not the case when the nonlinear estimator is first introduced in [6], which presents a good estimation performance. This phenomenon can be explained as follows. Unlike reference [6] which also adopts a weakly nonlinear model in the simulator, this paper applies a high-fidelity simulator which is expected to have a significant model mismatch compared to the weakly nonlinear model. Therefore, it is

understandable the excitation force is overestimated. This conclusion indicates that a data-driven approach (such as neural networks) for estimating the excitation force may have better performance when working with high fidelity simulations because it would have the capability of integrating all the measurements (including the pressure sensors measurements) without being restricted to a certain hydrodynamic model.

IV. Conclusion

The performance of a nonlinear excitation force estimator is assessed in this paper by using a high-fidelity simulator. The high-fidelity simulations are conducted in a Computational Fluid Dynamics based Numerical Wave Tank. The introduced estimator, which applies a weakly nonlinear model, collects the measurements in-line with the simulation. Numerical experiments are conducted, and the results show the nonlinear estimator overestimates the excitation force compared to the force extracted from a diffraction test. This overestimation can be explained by the significant model mismatch between the weakly nonlinear model and the numerical wave tank. Furthermore, this observation motivates the application of a data-driven approach that eliminates the restriction on a certain hydrodynamic model.

References

[1] B. Drew, A. R. Plummer, and M. N. Sahinkaya, "A review of wave energy converter technology," *Proceedings of the Institution of Mechanical Engineers, Part A: Journal of Power and Energy*, vol. 223, no. 8, pp. 887–902, 2009.

[2] J. Falnes, *Ocean waves and oscillating systems: linear interactions including wave-energy extraction*. Cambridge university press, 2002.

[3] S. Zou, O. Abdelkhalik, R. Robinett, G. Bacelli, and D. Wilson, "Optimal control of wave energy converters," *Renewable Energy*, vol. 103, pp. 217–225, 2017.

[4] G. Bacelli and J. V. Ringwood, "Numerical optimal control of wave energy converters," *IEEE Transactions on Sustainable Energy*, vol. 6, no. 2, pp. 294–302, 2015.

[5] S. Zou and O. Abdelkhalik, "Consensus estimation in arrays of wave energy converters," *IEEE Transactions on Sustainable Energy*, 2018.

[6] O. Abdelkhalik, S. Zou, R. Robinett, G. Bacelli, and D. Wilson, "Estimation of excitation forces for wave energy converters control using pressure measurements," *International Journal of Control*, vol. 90, no. 8, pp. 1793–1805, 2017.

[7] S. Zou and O. Abdelkhalik, "Time-varying linear quadratic gaussian optimal control for three-degree-of-freedom wave energy converters," *Renewable Energy*, vol. 149, pp. 217–225, 2020.

[8] Y. Peña-Sanchez, C. Windt, J. Davidson, and J. V. Ringwood, "A critical comparison of excitation force estimators for wave-energy devices," *IEEE Transactions on Control Systems Technology*, 2019.

[9] M. Garcia-Abril, F. Paparella, and J. Ringwood, "Excitation force estimation and forecasting for wave energy applications," *IFAC-PapersOnLine*, vol. 50, no. 1, pp. 14 692–14 697, 2017.

[10] H.-N. Nguyen and P. Tona, "Wave excitation force estimation for wave energy converters of the point-absorber type," *IEEE Transactions on Control Systems Technology*, 2017.

[11] B. Guo, R. J. Patton, S. Jin, and J. Lan, "Numerical and experimental studies of excitation force approximation for wave energy conversion," *Renewable Energy*, vol. 125, pp. 877–889, 2018.

[12] M. Abdelrahman, R. Patton, B. Guo, and J. Lan, "Estimation of wave excitation force for wave energy converters," in *Control and Fault-Tolerant Systems (SysTol), 2016 3rd Conference on*. IEEE, 2016, pp. 654–659.

[13] M. Penalba, A. Mérigaud, J.-C. Gilloteaux, and J. V. Ringwood, "Influence of nonlinear froude–krylov forces on the performance of two wave energy points absorbers," *Journal of Ocean Engineering and Marine Energy*, vol. 3, no. 3, pp. 209–220, 2017.

[14] G. Giorgi and J. V. Ringwood, "Nonlinear froude-krylov and viscous drag representations for wave energy converters in the computation/fidelity continuum," *Ocean Engineering*, vol. 141, pp. 164–175, 2017.

[15] Y.-H. Yu and Y. Li, "Reynolds-averaged navier–stokes simulation of the heave performance of a two-body floating-point absorber wave energy system," *Computers & Fluids*, vol. 73, pp. 104–114, 2013.

[16] M. Anbarsooz, M. Passandideh-Fard, and M. Moghiman, "Numerical simulation of a submerged cylindrical wave energy converter," *Renewable Energy*, vol. 64, pp. 132–143, 2014.

[17] T. Tezdogan, Y. K. Demirel, P. Kellett, M. Khorasanchi, A. Incecik, and O. Turan, "Full-scale unsteady rans cfd simulations of ship behaviour and performance in head seas due to slow steaming," *Ocean Engineering*, vol. 97, pp. 186–206, 2015.

[18] J. Palm, C. Eskilsson, G. M. Paredes, and L. Bergdahl, "Coupled mooring analysis for floating wave energy converters using cfd: Formulation and validation," *International Journal of Marine Energy*, vol. 16, pp. 83–99, 2016.

[19] C. Windt, N. Faedo, M. Penalba, F. Dias, and J. V. Ringwood, "Reactive control of wave energy devices–the modelling paradox," *Applied Ocean Research*, vol. 109, p. 102574, 2021.

[20] C. Windt, J. Davidson, and J. V. Ringwood, "High-fidelity numerical modelling of ocean wave energy systems: A review of computational fluid dynamics-based numerical wave tanks," *Renewable and Sustainable Energy Reviews*, vol. 93, pp. 610–630, 2018.

[21] F. ANSYS, "Fluent user's manual," *Software release*, vol. 13, 2006.

[22] B. A. Ling and B. A. Batten, "Real time estimation and prediction of wave excitation forces on a heaving body," in *ASME 2015 34th International Conference on Ocean, Offshore and Arctic Engineering*, vol. 9: Ocean Renewable Energy, no. OMAE2015-41087. St. Johns, Newfoundland, Canada: ASME, May 31June 5 2015.

[23] S. Zou and O. Abdelkhalik, "A numerical simulation of a variable-shape buoy wave energy converter," *Journal of Ocean Engineering and Marine Energy*, under review.

[24] J. L. Crassidis and J. L. Junkins, *Optimal estimation of dynamic systems*. CRC press, 2011.

[25] C. Windt, J. Davidson, D. D. Chandar, N. Faedo, and J. V. Ringwood, "Evaluation of the overset grid method for control studies of wave energy converters in openfoam numerical wave tanks," *Journal of Ocean Engineering and Marine Energy*, vol. 6, no. 1, pp. 55–70, 2020.

[26] M. A. Bhinder, M. Rahmati, C. G. Mingham, and G. A. Aggidis, "Numerical hydrodynamic modelling of a pitching wave energy converter," *European Journal of Computational Mechanics*, vol. 24, no. 4, pp. 129–143, 2015.